Chemical Engineering Journal 543 (2026) 178191

Contents lists available at ScienceDirect

Chemical Engineering Journal

journal homepage: www.elsevier.com/locate/cej

Kinetic investigation of methane pyrolysis over iron-based catalyst in packed bed reactor

Davide Cafaro [a], Marco Orsenigo [a], Veronica Piazza [a], Lidia Castoldi [a], Flavio Lucini [b], Andrea Lainati [b], Gianpiero Groppi [a], Matteo Maestri [a], Alessandra Beretta [a,*]

[a] Laboratory of Catalysis and Catalytic Processes, Dipartimento di Energia, Politecnico di Milano, via La Masa 34, Milano, 20156, Italy
[b] ENI – San Donato Research Center, ENI, 20097, Milan, Italy

ARTICLE INFO

Keywords:
Turquoise hydrogen
Methane pyrolysis
Kinetic investigation
Predictive kinetic model
Packed bed reactor
Iron-alumina catalyst

ABSTRACT

Methane pyrolysis emerges as a promising route to generate high-purity hydrogen and solid carbon without CO_2 emissions. This work investigates the kinetics of methane decomposition over a Fe-Al_2O_3 catalyst with equimolar Fe/Al ratio, synthesized via fusion-decomposition method and previously identified as the best formulation for activity and carbon accumulation capacity. Experiments were carried out in a packed bed reactor under widely varying operating conditions: temperature (725–800 °C), methane concentration (2.5–95% *v*/v), gas hourly space velocity (1000–100,000 L(NTP) h^{-1} kg_{cat}^{-1}), and hydrogen co-feeding (0–80% v/v). A one-dimensional dynamic reactor model was applied to develop a predictive kinetic model able to simultaneously describe methane conversion and catalyst deactivation as functions of operating conditions, and local gas-phase and solid phase composition. Specifically, the pyrolysis rate is described with a first-order dependence on methane partial pressure, while catalyst activity is modelled as a declining function of the locally accumulated carbon, a property of the solid that varies spatially and dynamically across the reactor and the time on stream. The model combines formal simplicity with the capability to accurately reproduce methane conversion, hydrogen productivity, and carbon load and distribution under all tested conditions. Surface maps of carbon deposition and catalyst activity across the reactor length could be generated, offering predictive insights valuable for the design of experiments, including strategies for long lasting runs. The results of this study underscore the potential of Fe-based catalysts for CO_2-free hydrogen production at the industrial scale and provide rate equations validated over an operating field of unprecedented extension, that are expected to enable the scaling up of methane pyrolysis technologies.

1. Introduction

In recent years, the scientific community has increasingly focused the attention on the pressing issues of environmental pollution and climate change. Today, fossil fuels such as natural gas, oil, and coal remain the primary energy sources for heat and power generation [1]. However, their thermal conversion results in the release of significant amount of greenhouse gas (GHG) emissions. This has created an urgent need to develop technologies capable of producing alternative, cleaner fuels.

A promising solution is the adoption of hydrogen as a clean energy source, since its combustion for heat and electricity generation produces only water as by product [2], with no carbon dioxide emissions [3,4]. As a result of its expanding range of applications, global hydrogen demand has grown significantly, increasing from 18.2 million tons (Mt) in 1975 to 100 Mt. in 2024 [5].

However, global hydrogen production still relies on fossil fuels. Currently, hydrogen is mainly produced through steam methane reforming (SMR: $CH_4 + H_2O \leftrightarrow CO + 3H_2$, referred to as grey hydrogen) or coal gasification (brown/black hydrogen). These processes generate substantial GHG emissions - around 830 Mt./y of CO_2 [6,7] - requiring technologies for carbon capture and storage (CCS, blue hydrogen), increasing the hydrogen production cost (2–3€/kg-H_2) [8]. Alternatively, carbon-free hydrogen can be produced through water electrolysis using electricity generated from renewable sources (green hydrogen) or nuclear power (purple hydrogen), though this technology is not yet economically competitive [6]. Indeed, SMR produces H_2 for less than $2/kg [9], whereas water electrolysis powered by renewable electricity can cost $4–$15 per kg of H_2 [10,11].

Therefore, there is a critical need to develop new hydrogen production processes that are both carbon-free and economically

* Corresponding author.
E-mail address: alessandra.beretta@polimi.it (A. Beretta).

https://doi.org/10.1016/j.cej.2026.178191
Received 10 January 2026; Received in revised form 9 May 2026; Accepted 7 June 2026
Available online 8 June 2026

Nomenclature

$a(t,w)$	catalyst activity
a_∞	residual catalyst activity
$\alpha,\beta,\gamma,\delta$	coefficients of the polynomial expression for the average temperature
b	deactivation order with respect to methane
C_{local}	local carbon load, C-load, defined as mass of C accumulated per mass of reduced catalyst $kg_C\ kg_{catR}^{-1}$ at the generic axial coordinate, at time t
$C_{reactor}$	Integral reactor carbon load, C-load, defined as mass of C per mass of reduced catalyst $kg_C\ kg_{catR}^{-1}$ accumulated in the whole bed at time t
d	deactivation order with respect to catalyst activity
E_a	activation energy, kJ mol^{-1}
$E_{a,p}$	activation energy for pyrolysis, kJ mol^{-1}
$E_{a,d}$	activation energy for deactivation, kJ mol^{-1}
i	index identifying the i-th gaseous species
j	denotes either p or d, referring to pyrolysis or deactivation
k_d	deactivation constant, $kg_{catR}\ kg_C^{-1}$
K_{eq}	equilibrium constant of methane pyrolysis
K_p	reaction quotient
k_p	pyrolysis kinetic constant, mol s^{-1} kg_{catR}^{-1} atm^{-1}
M_i	molar mass, kg $kmol^{-1}$
m_C	mass of deposited carbon, kg
$m_{cat,R}$	mass of reduced catalyst, kg
$\dot{m}_i$	mass flowrate, kg s^{-1}
$\dot{n}_i^{in}$	inlet molar flow rate, mol s^{-1}
$\dot{n}_i^{out}$	outlet molar flow rate, mol s^{-1}
n	reaction order
ΔP_{exp}	experimental Pressure drop, atm
P	pressure, atm
P_i	partial pressure, atm
r_d	deactivation reaction rate, s^{-1}
r_p^0	methane pyrolysis reaction rate at time zero, mol s^{-1} kg_{catR}^{-1}
$r_p(t)$	methane pyrolysis reaction rate, mol s^{-1} kg_{catR}^{-1}
R	universal gas constant, J mol^{-1} K^{-1}
t	time, s
T	operating temperature, K
T_{ref}	reference temperature, K
ν_i	stoichiometric coefficient
w	integration coordinate across the catalyst mass, kg_{catR}
W_{TOT}	total catalyst mass, kg_{catR}
η	ratio between the reaction quotient and the equilibrium constant

Abbreviations

cat	catalyst
CCS	carbon capture and storage
CSTR	continuous stirred tank reactor
Exp	experimental
GHG	greenhouse gas emissions
GHSV	gas hourly space velocity
Mt	million tons
PDE	partial differential equations
Ref	Reference
SCS	solution combustion synthesis
SMR	steam methane reforming
TOS	time on stream
WI	wet impregnation

competitive. One such alternative is methane pyrolysis, which enables the production of high purity H_2 (turquoise hydrogen) and solid carbon without the direct release of CO_2, [12]: ($CH_4 \rightleftarrows 2H_2 + C$, ΔH_R^0 (298K) = 75 kJ/mol).

This process requires around 37.5 kJ per mole of H_2 produced, that is lower than 286 kJ required for water electrolysis and 63.4 kJ needed for SMR [13,14].

Moreover, the solid carbon produced can be valorized, improving the economic feasibility of the process. The literature documents applications of the carbon product as a catalyst [15], as a precursor for graphitic materials [16], in composites, bi-layer capacitors [17], or to produce advanced materials (e.g., carbon nanotubes fibers) with structural integrity, which can replace traditional materials like aluminum and copper due to their improved mechanical and conductive properties [18,19]. A promising application of the carbon rich solids is then represented by the self-reducing C-agglomerates for the steel industry [20].

Methane pyrolysis is an endothermic process that requires temperatures above 1000 °C to break the C—H bond and reach sufficient conversion rates [21,22]. For this reason, the use of a catalyst can enhance the reaction kinetics, thereby lowering the required operating temperature [23–26].

The common catalysts used for methane pyrolysis are transition metals such as nickel (Ni), iron (Fe) and cobalt (Co), supported over metal oxides like Al_2O_3, MgO or SiO_2 [23,27,28]. Among these, Ni- and Co-based catalysts are the most active but tend to deactivate quickly at temperature above 600 °C due to coking [29,30]. Furthermore, at this temperature, the maximum achievable methane conversion is relatively low (approximately 60%), which leads to high separation costs for the outlet methane-hydrogen mixture. Ni- and Co-based catalysts are also limited in application due to their heavy-metal toxicity and potential harmful effects on human beings [31].

In contrast, Fe-based catalysts are receiving increasing attention as a viable alternative. Although they exhibit lower activity compared to Ni- or Co-based catalysts, they are more abundant, less expensive, and less prone to sintering at higher temperatures [32,33].

Despite this, the reaction kinetics and deactivation mechanisms of methane pyrolysis over Fe-based catalysts remain underexplored. The earliest study, conducted by Grabke et al. in 1970 [34], investigated methane cracking over iron supported on γ-alumina and proposed a detailed reaction mechanism, consisting of methane stepwise dehydrogenations, ultimately forming dissolved carbon, carbon filaments and encapsulating carbon blocking the active sites [35].

Geng et al. [36] investigated the kinetics of methane decomposition over a 20 wt% Fe-based catalyst in a micro fluidized bed reactor. Pulse catalyst injection into a fluidized bed was adopted as testing methodology, as it ensured isothermal conditions and minimized both internal and external mass-transfer limitations. However, the analysis of experimental rate data indicated a reaction order with respect to methane partial pressure of 2.27 and an apparent activation energy of 50 kJ mol^{-1}, which appear mainly empirical being hardly consistent with a physico-chemical justification. Catalyst deactivation was modelled using the power-law expression $-\frac{da}{dt} = k_d P_{CH_4}^m a^d$. Optimal deactivation order (d = 1.8) and order of the deactivation rate on methane partial pressure (m = 0.95) were also obtained from the experiments. A large activation energy for the deactivation constant (E_d = 121.37 kJ mol^{-1}) was then introduced to describe the effect of temperature on the activity decay.

Keller et al. [37] studied methane decomposition kinetics in a laboratory-scale quartz fluidized bed reactor (35 mm i.d.) operated at atmospheric pressure and temperatures between 750 and 900 °C. The reactor contained 25 g of spray-dried Fe_2O_3/Al_2O_3 catalyst, and the inlet gas mixture consisted of methane and nitrogen (10–40% CH_4). The

kinetic analysis of the dynamic response of the reactor was based on a back-mixed reactor (CSTR) model; a reaction order of 0.63 was estimated with apparent activation energy of 128.1 kJ mol^{-1} below 800 °C and 21.5 kJ mol^{-1} above 800 °C, indicating mass transfer limitations at higher temperatures. Catalyst deactivation was found to proceed linearly with carbon deposition and to be temperature-independent, suggesting that deactivation was primarily governed by carbon accumulation rather than thermal sintering. Notably, in order to preserve the structural integrity of the catalyst particles, the experiments were conducted at very low C-load, up to a maximum of 10 wt-% relative to the catalyst mass.

Siriwardane et al. [38] studied the performance of a Fe/Al_2O_3 in methane and ethane cracking. Thermogravimetric analyses under isothermal conditions were used to quantify the rate of reaction under conditions of quasi steady-state performance that established after an initial transient behavior. Experimental data were fitted by a power-law model of the form $r = kp^n_{C_xH_y}$. For methane pyrolysis, an apparent activation energy of 43.2 kJ mol^{-1} and a reaction order of 0.6 were obtained. Ethane pyrolysis exhibited a higher activation energy of 62.2 kJ mol^{-1} and the same reaction order. The authors emphasized that the proposed Fe/Al_2O_3 catalyst showed remarkable stability, when operated in fluidized bed reactor, maintaining methane conversion above 80% for more than 160 h and above 60% for 224 h of continuous operation; however, it must be observed that the operating conditions selected (low total flow rate and highly diluted feed) were such to minimize the rate of carbon accumulation.

The most recent study by Vedele et al. [39] examined four alumina-supported iron catalysts, synthesized via wet impregnation (WI) and solution combustion synthesis (SCS), with iron oxide loadings of 60 wt% and 40 wt%. Kinetic tests on the higher iron-loaded samples were conducted in a quartz fixed bed reactor, selecting suitable operating conditions to minimize the deactivation phenomena (with 3.5 vol% methane in inert feeds at 610–700 °C). Results showed that SCS-derived materials exhibited better catalytic performance, attributed to a larger iron dispersion, reduced sintering, and the formation of a mixed $FeAl_2O_4$ phase, which enhances thermal stability. Methane conversion was higher and more stable for the SCS catalysts, which also exhibited a lower activation energy (133 kJ mol^{-1} vs. 160 kJ mol^{-1} for WI).

A certain degree of scatter in the kinetic results emerges from the literature, where kinetic models and parameters (reaction orders, activation energy) appear associated to the specific catalysts, the operating field, the experimental set-up. The development of an intrinsic and predictive kinetic model adequate to describe the dynamic process over a wide operating field is still missing, although necessary for any reactor design applications. This is the very open gap that the present study aims to close.

In a previous work by the authors [40], Fe-Al_2O_3 catalysts at increasing iron content were synthetized via fusion-decomposition method and extensively characterized. Based on the results of characterization, activity screening in thermobalance and in packed bed reactor, the Fe-Al_2O_3 catalyst with equimolar Fe/Al ratio showed the best performances in terms of carbon accumulation capacity and hydrogen productivity owing to its favorable textural and structural properties.

The same equimolar Fe-Al_2O_3 catalyst is herein adopted for a detailed kinetic investigation of methane pyrolysis over a very wide operating field, with the aim of extracting the dominant kinetic dependencies. Experiments were performed in a packed bed reactor at varying temperatures (725–800 °C), inlet methane composition (2.5–95% *v*/v), gas hourly space velocity (GHSV 1000–100,000 L(NTP) h^{-1} kg^{-1}_{cat}), and H_2 co-feed (0–80% v/v). A one-dimensional dynamic reactor model was applied to the quantitative analysis of the data and the development of an intrinsic kinetic model able to describe the effects of the operating conditions.

Reactor and kinetic models were then used to identify the operating conditions that slow down catalyst deactivation and maximize its carbon accumulation capacity. Indeed, maximizing the cumulated C is essential to extend catalyst lifetime, a key parameter for enhancing efficiency and economics of the catalytic pyrolysis process [41].

2. Experimental methodology

2.1. Catalyst preparation and characterization

Pyrolysis experiments were performed on a Fe-Al_2O_3 catalyst with an equimolar Fe/Al ratio (corresponding to an iron load of 52 wt%). The catalyst was prepared via fusion-decomposition method [42], using aluminum nitrate nonahydrate and iron nitrate nonahydrate as salt precursors. These salts were calcined in air following a two-ramp heating program: 3 °C min^{-1} to 350 °C (1 h hold), then 5 °C min^{-1} to 450 °C (8 h hold). Fresh (i.e., after calcination) and reduced (i.e., after the reduction treatment explained in **Section 2.2**) samples were characterized with N_2 adsorption-desorption, X-Ray diffraction, FESEM and HRTEM, as presented in detail by the authors in a previous study [40]. In summary, the catalyst used for this work revealed a BET surface area of 125 m^2 g^{-1} in the fresh form, with mesoporous Fe_2O_3 aggregates dispersed in microporous amorphous Al_2O_3. After reduction, the surface area decreased to 52 m^2 g^{-1}, with metallic Fe^0 aggregates still dispersed in the alumina with iron crystallites of 28 nm.

2.2. Experimental setup and operating conditions

Experiments of CH_4 pyrolysis were conducted in a laboratory scale packed-bed reactor made of quartz (I.D. 15.0 mm), where the catalyst was tested in the powder form with particle size in the 200–500 μm. To minimize overpressure caused by carbon deposition and to contrast the endothermic nature of pyrolysis reaction, the catalytic bed was diluted with quartz grains of the same size at 1:15 dilution ratio by weight. In each experiment, the reactor was loaded with 0.75 g of catalyst and 11.25 g of quartz which resulted in bed length of about 50.0 mm and average bulk density of 1200.0 kg m^{-3} (Fig. 1a). The only exceptions were pyrolysis tests conducted at Gas Hourly Space Velocity (GHSV) of 40,000 and 100,000 L(NTP) h^{-1} kg^{-1}_{cat}, which were carried out in a smaller packed-bed reactor (I.D. 10.0 mm) loaded with 0.125 and 0.051 g of catalyst, respectively. Quartz dilution ratio was also reduced down to 1:5 by weight.

The catalytic bed was positioned between two layers of quartz wool. An additional column of quartz grains (850.0–1200.0 μm) was loaded above the bed to promote uniform gas distribution and temperature profile. The reactor was inserted into an electrically heated tubular oven where the catalytic bed was positioned within the isothermal zone of the oven (Fig. 1b). Axial temperature profiles were measured during the tests by sliding a K-thermocouple inserted inside a central thermowell whereas pressure drops across the reactor were monitored using a pressure transducer (STS) installed upstream the reactor.

Feed gases such as CH_4, N_2, and H_2 were flown to the reactor using mass flow controllers (Brooks®) via stainless steel lines (O.D. 1/4 “) heated at 120 °C. Downstream the reactor, gas composition was analysed using an online micro-GC 3000 A (Agilent Technologies) equipped with a Molecular Sieve column, a PlotU capillary column and TCD detectors; N_2 was used as internal standard for quantitative analysis. Gas sampling and analysis was performed with a frequency of 1/3 min^{-1}, which was fully compatible with the velocity of the observed dynamics.

Before pyrolysis tests, the catalyst was reduced at 550 °C (5 °C min^{-1} heating followed by 1 h hold at 550 °C) sending a mixture of concentrated hydrogen (75 vol% H_2 in N_2) at GHSV of 40,000 L(NTP) h^{-1} kg^{-1}_{cat}. Then, the catalyst was heated at 800 °C (10 °C min^{-1} heating followed by 30 min hold) and brought to the pyrolysis temperature under pure N_2 flow. Pyrolysis tests were carried out by subjecting the catalytic bed to the reacting mixture for a prolonged time and monitoring the dynamic evolution of the outlet mixture composition and pressure, while keeping

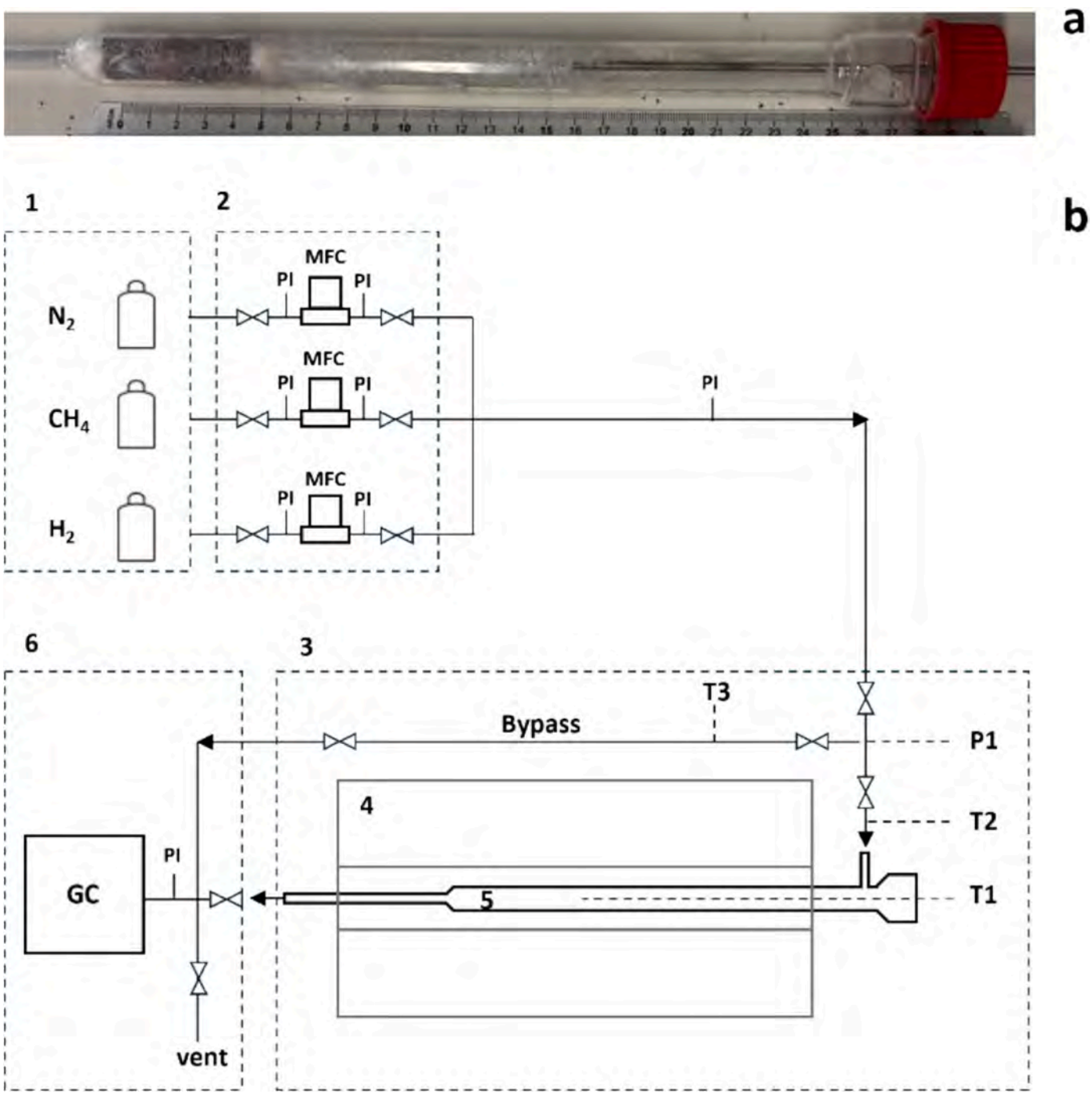

Fig. 1. (**a**) Schematic representation of laboratory-scale pyrolysis test rig: (1) pressurize vessels for nitrogen (N_2), methane (CH_4), hydrogen (H_2) storage (200 bar); (2) feeding section with flow control through mass flow controllers (MFC, *Brooks*®). Pipe pressure is monitored with specific pressure gauges (PI). (3) Reaction section provided with (4) an electrically heated tubular oven, (5) tubular reactor, a K-type thermocouple (T1), pressure transmitter (P1, *STS*), and an additional reactor bypass line (bypass). Both reactor and bypass lines are heated by means of heating tapes whose temperature is controlled with K-type thermocouples (T2, T3). (6) Analysis section equipped with an online gas chromatograph (GC, *micro-GC 3000 A, Agilent Technologies*) and vent line (vent). (**b**) Picture of the packed-bed reactor adopted in the experimental campaign.

constant the temperature and the inlet stream. The reaction was explored under a wide range of conditions such as inlet gas composition (2.5–95.0 vol% CH_4 in N_2), GHSV (1000–100,000 L(NTP) h^{-1} kg_{cat}^{-1}), inlet H_2 co-feeding (0–40 vol% H_2 in CH_4 and N_2) and temperature (725–800 °C).

From each experiment, CH_4 conversion, C-load and H_2 productivity were evaluated.

At the generic time t, CH_4 conversion was determined by comparing the measured inlet ($\dot{n}_{CH4}^{in}$) and outlet ($\dot{n}_{CH4}^{out}$) molar flow rates of methane as reported in **Eq. (1)**:

$$CH_4\ conversion = \frac{\dot{n}_{CH4}^{in} - \dot{n}_{CH4}^{out}}{\dot{n}_{CH4}^{in}} \quad (1)$$

Methane conversion was also independently evaluated using the inlet and outlet molar flow rates of hydrogen. The values obtained through both methods, based on methane and hydrogen flow rates, were

found to be mutually consistent, thereby validating the reliability of the experimental data.

The integral C-load accumulated within the reactor ($C_{reactor}$, $g_C\ g_{catR}^{-1}$) was then computed as the ratio between the mass of deposited carbon (m_C) until time t and the mass of reduced catalyst ($m_{cat.R}$) in the bed, according to **Eq. (2)**. The total mass of deposited carbon was calculated as difference between the inlet and outlet carbon flows to close the carbon balance.

$$C_{reactor} = \frac{m_C}{m_{catR}} \tag{2}$$

As third dynamic key performance indicator, H_2 productivity ($gH_2\ h^{-1}\ g_{catR}^{-1}$) was computed as the ratio between the measured mass flowrate of produced H_2 ($\dot{m}_{H_2}^{out} - \dot{m}_{H_2}^{in}$) and the mass of reduced catalyst ($m_{cat.R}$), as reported in **Eq. (3)**.

$$H_2\ productivity = \frac{\dot{m}_{H_2}^{out} - \dot{m}_{H_2}^{in}}{m_{cat.R}} \tag{3}$$

3. Modelling methods

A one-dimensional, pseudo-homogeneous, dynamic packed bed reactor model was developed to describe methane decomposition and catalyst deactivation as functions of time and position along the catalytic bed.

The complete set of governing equations is reported in Table 1, including boundary and initial conditions. Material balances for gas-phase species were formulated according to the 1D pseudo-homogeneous PFR model. A material balance for the solid phase was introduced to account for the accumulation of solid carbon on the catalyst. It was assumed that the characteristic timescale of the gas-phase dynamics is significantly shorter than that of carbon deposition; therefore, the transient accumulation term for the gas phase was neglected, corresponding to a steady-state gas-phase assumption.

The reaction kinetics were described by following a widely adopted approach in the literature [43], that is by expressing the reaction rate under deactivation as the product of the initial rate and a space– and time-dependent catalyst activity function, as shown in **Eq. (4)**:

$$r_p(t) = a(t,w) \bullet r_p^0 \bullet (1-\eta) \tag{4}$$

where the term $(1-\eta)$ accounts for the thermodynamic consistency, being η the ratio between the experimental quotient K_p (assuming ideal gas behavior) and the thermodynamic equilibrium constant K_{eq}. This in turn is calculated by minimizing the total Gibbs free energy of the system, assuming the thermodynamic properties from [44], with C as graphitic carbon.

Within the model, it is assumed that the spatial and time-dependence of catalyst activity function a affects the evolution of the axial profiles of gas-phase species and solid carbon; its dynamic evolution is introduced by the definition of a deactivation rate, r_d, as shown in Table 1.

In this work, the kinetic expressions of both r_p^0 and a were developed based on experimental evidence and are discussed in the following sections.

The temporal evolution of pressure and temperature were also considered, by using the empirical analytical expressions reported in Table 1. The pressure profile was approximated as linear along the catalyst bed and fitted to the measured pressure drop. Isothermal conditions were assumed along the reactor axis, with a time-dependent temperature, which was described by fitting the measured average bed temperature with a third-degree polynomial function.

The resulting system of partial differential equations (PDEs) was implemented in Matlab® and numerically solved using the fsolve function [45]. Details on the numerical procedure are provided in the Supporting information, **Section SI.1.1**.

Table 1
Model equations of the 1-D dynamic packed bed reactor.

Gas phase mass balance equation of species i
$-\frac{d\dot{m}_i}{dw} + \nu_i r_p(t) M_i = 0 \quad \forall w \in [0,W]$ with $\dot{m}_i(w=0) = \dot{m}_i^{IN}\ \forall t \in [0,t]$\vskip2pt
Solid phase mass balance equation
$-\frac{\partial C_{local}}{\partial t} + r_p(t) MM_C = 0 \quad \forall t \in [0,t]$ with $C_{local}(t=0) = 0\ \forall w \in [0,W]$
Equation for the catalyst activity
$-\frac{\partial a}{\partial t} - r_d = 0 \quad \forall t \in [0,t]$ with $a(t=0) = 1$
Pressure profile fit
$P(t,w) = P_{OUT} + \frac{\Delta P_{exp}(t)}{W_{TOT}}(W_{TOT} - w)$
Temperature profile fit
$T = \alpha t^3 + \beta t^2 + \gamma t + \delta$

4. Results and discussion

4.1. Pyrolysis experiments in packed bed reactor

Fig. 2 shows the results of a reference pyrolysis test conducted at the operating temperature of 800 °C and atmospheric pressure, feeding a gas mixture containing 40% CH_4 balanced with N_2 at GHSV of 20,000 L (NTP) $h^{-1}\ kg_{cat}^{-1}$. The panels show the set of measurements and key performance indicators that characterize the single test, thus the outlet gas composition (CH_4, H_2 and CO), CH_4 conversion, the global $C_{reactor}$ and H_2 productivity. Temporal evolutions of pressure drop and average temperature along the axial coordinate of the reactor were observed and are provided in **Figs. SI.2** and **SI.3** of the Supplementary Information.

During the reaction, typical trends are observed; the molar fraction of CH_4 increases with time on stream (TOS), while the molar fraction of H_2 decreases but does not reach zero, suggesting that some residual conversion persists (Fig. 2a). CO is also detected in the product mixture (Fig. 2a) still declining with TOS; its presence in the product mixture may be attributed to a residual fraction of oxidized catalyst still present after the reduction step. In our previous study [40], based on independent characterization measurements, it was estimated that about 15% of iron is present in the form of $FeAl_2O_4$ after the reducing pre-treatment (details of the calculations are provided in the Supplementary Information, **Section SI.2.1**). Indeed, the global amount of CO detected during the run is consistent with such estimate.

Fig. 2b and Fig. 2c present the resulting decreasing profiles of CH_4 conversion and hydrogen productivity over time, highlighting the phenomenology of catalyst deactivation due to carbon deposition. The decline trends are steeper in the early phase of the experiments, while they mitigate with time on stream, such that the reactor performance eventually reaches a sort of steady state. Consistently, the $C_{reactor}$ (Fig. 2c) increases more rapidly in the initial stages while, with time on stream, the incremental carbon accumulation also declines, and the global accumulated carbon grows linearly (but to a small extent) with time on stream.

4.1.1. Effect of inlet methane concentration

The influence of CH_4 inlet concentration was investigated in the range 20–95%; the results are reported in Fig. 3. All experiments were carried out under atmospheric pressure, an operating temperature of 800 °C and a GHSV of 20,000 L(NTP) $h^{-1}\ kg_{cat}^{-1}$. Fig. 3a shows that CH_4 conversion decreased importantly with increasing CH_4 feed. Still, both the $C_{reactor}$ (Fig. 3b) and H_2 productivity (see Supplementary Information**, Fig. SI.5a**) showed the opposite trend reflecting progressively higher converted CH_4 molar flows with increasing concentration of the feed. As a consequence, operating at high CH_4 inlet concentrations (e.g. 80–95%) also promoted faster catalyst deactivation and faster pressure rise in the reactor (see Supplementary Information, **Fig. SI.5b**).

In all the experiments, methane conversion did not fall to zero but

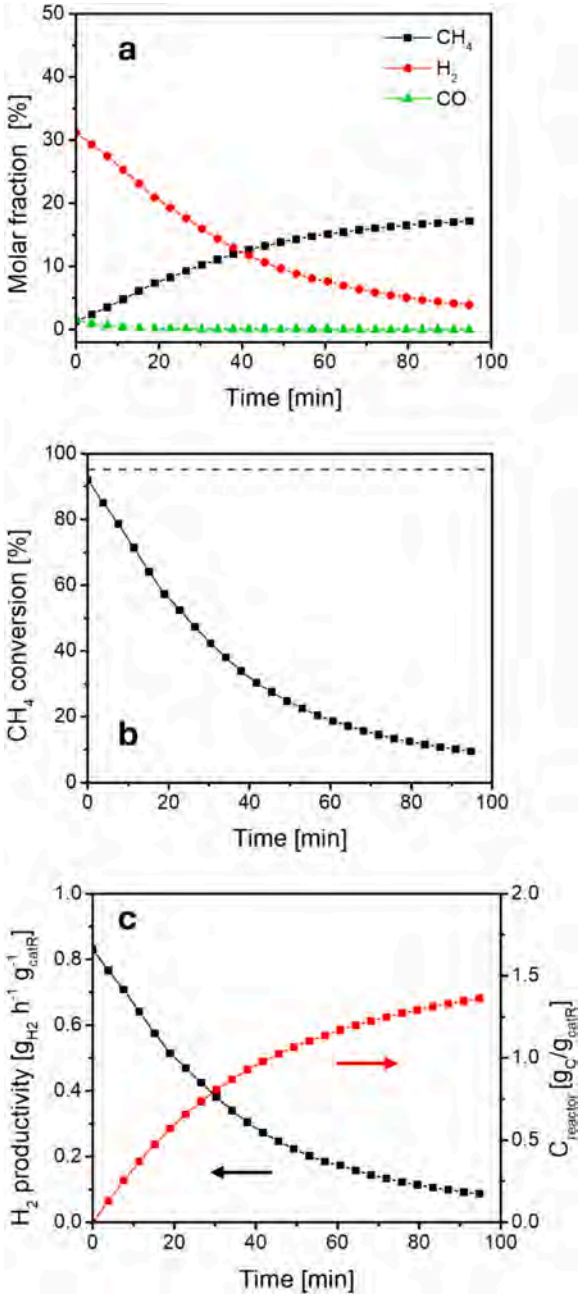

Fig. 2. Evolution over time on stream of CH_4, H_2 and CO molar fractions (a), CH_4 conversion (b), solid carbon production and H_2 productivity (c). Experimentally measured CH_4 conversion (line + symbols) and thermodynamic equilibrium CH_4 conversion (dashed line) are both reported (b).Operating conditions: $T = 800$ °C, GHSV = 20,000 L(NTP) h^{-1} kg_{cat}^{-1}. $CH_4 = 40\%$ *v*/v, N_2 to balance, atmospheric pressure. Experimental data are shown (line + symbols).

tended to approach an asymptotic value. This residual activity may be attributed to the activity of residual accessible iron particles not encapsulated by carbon nano-onions or nanotubes [46], while the contribution of thermal pyrolysis of methane is excluded under the explored conditions, as verified in a blank experiment reported in the Supplementary Information, **Fig. SI.4**.

4.1.2. *Effect of temperature*

Fig. 4 shows the results of experiments performed at varying temperature between 725 °C and 800 °C, while feeding 40% of CH_4 balanced with N_2, at constant GHSV of 10,000 L(NTP) h^{-1} kg_{cat}^{-1} and atmospheric pressure. Growing temperatures significantly affected CH_4 conversion (Fig. 4a), resulting in increasing initial conversions, but also in faster catalytic deactivation. Indeed, the conversion curves obtained at lower temperatures intersect those measured at higher temperatures, such that an inverse effect of temperature is shown after about 60 min, when greater conversion values are observed at lower temperatures. Similar trends are observed for calculated $C_{reactor}$ (Fig. 4b) and H_2 productivity (see Supplementary Information, **Fig. SI.6**).

These results highlight a different catalyst deactivation rate depending on the temperature, which likely reflects the effect of temperature on the carbon organization patterns, as better discussed in **Section 4.2**.

4.1.3. *Effect of hydrogen co-feeding*

The influence of hydrogen cofeed was also investigated at two different inlet hydrogen concentrations (i.e. 15% and 40%) balanced with CH_4/N_2 mixtures of 40%/20% and 80%/5% v/v, respectively. Both tests were conducted at the operating temperature of 800 °C and GHSV of 20,000 L(NTP) h^{-1} kg_{cat}^{-1} and were compared to reference experiments with the same inlet methane concentrations (i.e., 40% and 80% CH_4, respectively) in Fig. 5 and **Fig. SI.7** of the Supplementary Information. A slight increase of the initial methane conversion is observed when 40% H_2 is introduced into the feed as shown in Fig. 5 but the effect becomes negligible at 15% H_2 cofeed (see Supplementary Information, **Fig. SI.7**). Overall, the impact of hydrogen co-feeding on the methane pyrolysis rate appears to be moderate when compared with the effect of inlet methane concentration. Several kinetic studies have investigated the role of hydrogen in catalytic methane pyrolysis. However, highly scattered results have been reported depending on the catalyst and operating conditions; with both positive [47] and negative [48] H_2-dependences. In the present study, these results indicate that, under the tested conditions, the presence of hydrogen does not significantly influence the reaction rate.

4.1.4. *Effect of space velocity*

Fig. 6 illustrates the effect of GHSV on methane conversion in the range 5000 to 100,000 L(NTP) h^{-1} kg_{cat}^{-1}, feeding a mixture of 40% CH_4 balanced with N_2, at operating temperature of 800 °C and atmospheric pressure. At decreasing flow rate and GHSV, the initial methane conversion increased with a progressively closer approach to thermodynamic equilibrium. Besides, due to the decline of converted CH_4 molar flows and thus lower carbon accumulation rates (see Supplementary Information, **Fig. SI.8**), conversion was increasingly sustained in time.

It is interesting to observe that at the highest GHSV tested (40,000 and 100,000 L(NTP) h^{-1} kg_{cat}^{-1}), the reactor moved into a differential regime, thus revealing kinetic effects at the particle scale (decoupled from the reactor scale); here, the conversion curves show a peculiar trend, characterized by an initial delay, such that a declining trend is observed only after about 6 min of time on stream. We can speculate that this phenomenon is associated to the initial activation of the catalyst, involving the transformation of iron into iron carbide (Fe_3C), which acts as the active state of the catalyst in methane activation and carbon deposition [49]. Although a crucial step for the process, when operating the reactor at lower GHSV of practical interest, the longer contact time and the integral regime make the overall reactor response little sensitive to such initial transformation, being prevalent in time the global deactivation trend.

The effect of GHSV was also investigated at the temperature of 750 °C, as documented in the in the Supplementary Information, **Fig. SI.9**. The same qualitative trends were observed; however, lower initial conversion values and slower catalyst deactivation were observed in agreement with the temperature effect discussed above.

4.2. *Development of the kinetic model*

The experimental data above illustrated were fitted to derive the

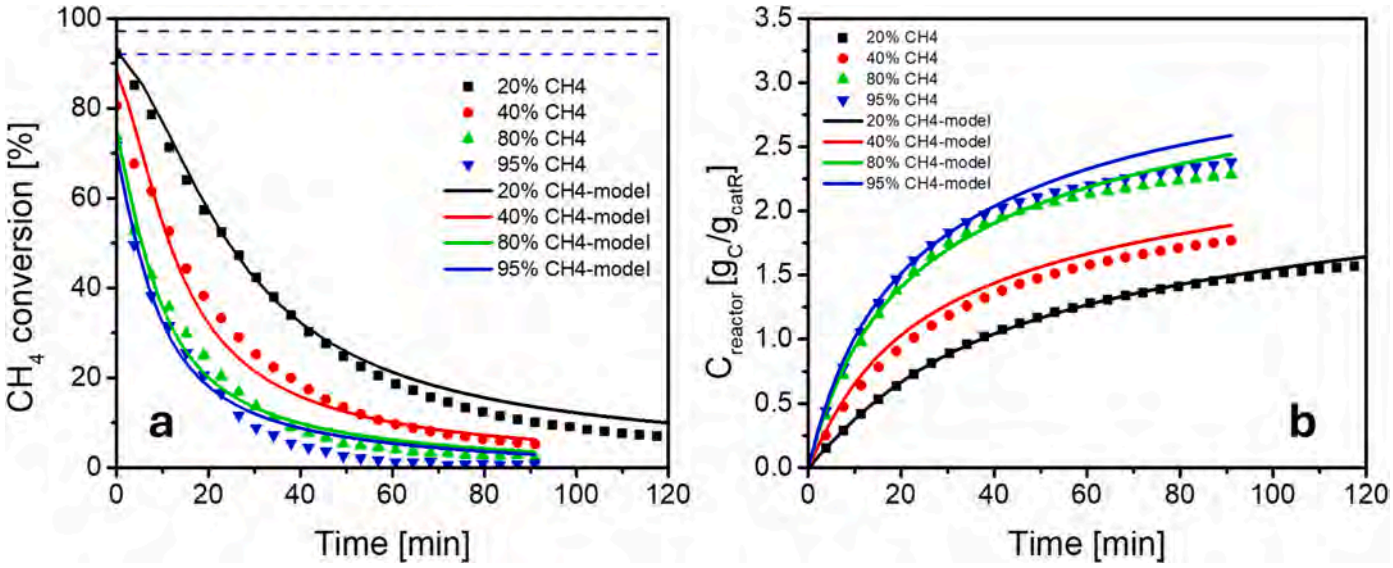

Fig. 3. Effect of inlet CH_4 concentration on: (a) CH_4 conversion and (b) solid carbon production. Experimental data (symbols) and calculated results (solid lines) are shown. Thermodynamic equilibrium CH_4 conversion (dashed line) is also reported (a). Operating conditions: $T = 800$ °C, GHSV = 20,000 L(NTP) h^{-1} kg_{cat}^{-1}. $CH_4 = 20$, 40, 80, 95% *v*/v, N_2 to balance, atmospheric pressure.

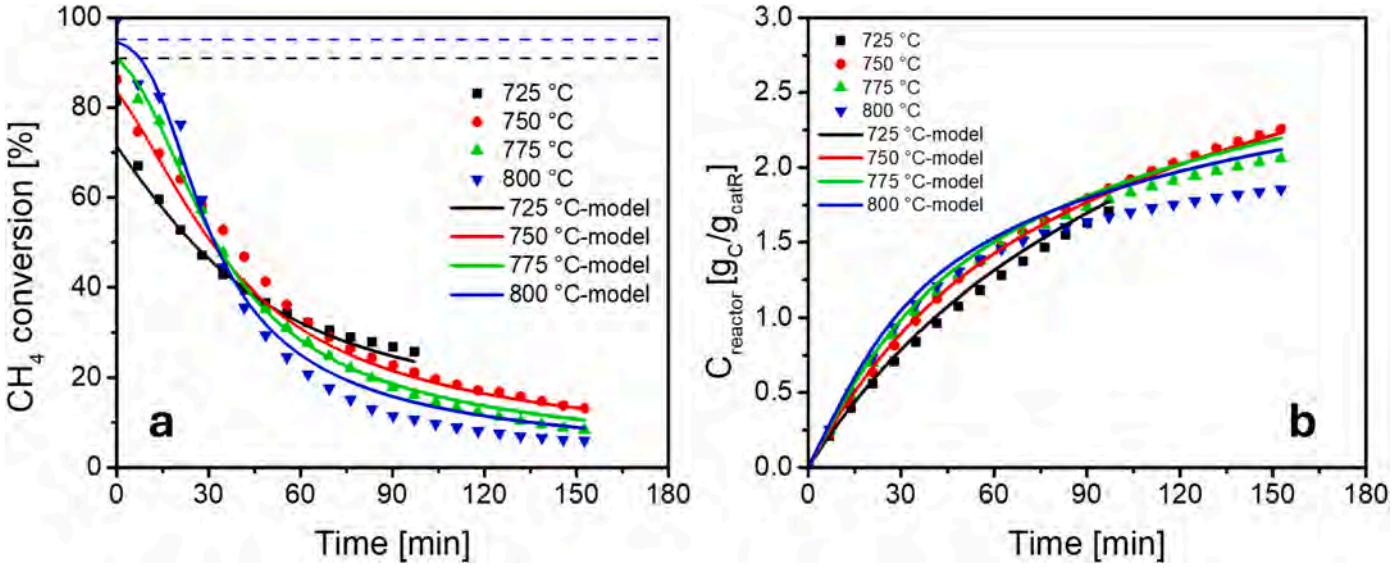

Fig. 4. Effect of temperature on: (a) CH_4 conversion and (b) solid carbon production. Experimental data (symbols) and calculated results (solid lines) are shown. Thermodynamic equilibrium CH_4 conversion (dashed line) is also reported (a). Operating conditions: temperature = 725, 750, 775, 800 °C, GHSV = 10,000 L(NTP) h^{-1} kg_{cat}^{-1}, CH_4 = 40% *v*/v, N_2 to balance, atmospheric pressure.

kinetic expression of the initial reaction rate r_p^0 and the deactivation rate r_d, which governs the evolution of the catalyst activity function a. Rate expressions and kinetic parameters are reported in Table 2.

Kinetic orders in r_p^0 were estimated from the measured initial hydrogen productivity at varying feed composition. The reaction order with respect to methane was estimated from the initial data at varying inlet methane concentration to 0.95 (**Fig. 7a**), which can be reasonably rounded to 1, consistently with values reported in the literature [50–53]. Details about data selection and mathematical elaboration are provided in the Supplementary Information. Given the moderate effect of H_2 cofeed, a zero-reaction order with respect to hydrogen was then assumed.

The formulation of a model for the activity decay relied on the observation that the dynamics of H_2 productivity normalized with respect to its initial value (which, by definition, represents the average activity of the bed) are far more strongly affected by the experimental descriptor of the carbon accumulation, rather than by the gas-phase composition. This is evident in **Fig. 7b**, obtained from the data at varying inlet CH_4 concentration, especially below 0.8 g_C g_{cat}^{-1} of overall cumulated carbon. This trend was translated into a local formulation by relating the activity of the particle to its carbon coverage (C_{local}). Consequently, a functional form for the catalyst activity explicitly accounting for the dependence on the local carbon coverage was adopted as shown in **Eq. (5)**.

$$\frac{a - a_\infty}{1 - a_\infty} = \exp(-k_d C_{local}) \tag{5}$$

where the progressive accumulation of carbon at the generic axial coordinate of the reactor is accounted for by the mass balance equation of the solid phase (Table 1). It is important to emphasize that C_{local} differs

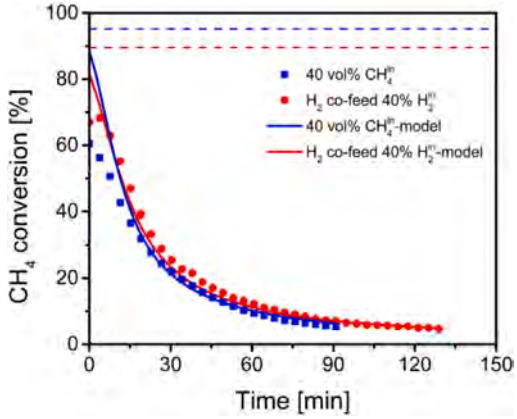

Fig. 5. Effect of H_2 co-feed on CH_4 conversion. Experimental data (symbols) and calculated results (solid lines) for CH_4 conversion. Thermodynamic equilibrium CH_4 conversion (dashed line) is also reported. Operating conditions: GHSV = 20,000 L(NTP) h^{-1} kg_{cat}^{-1}, temperature = 800 °C, atmospheric pressure, CH_4 = 40% *v*/v, H_2 = 40%, N_2 = 20%.

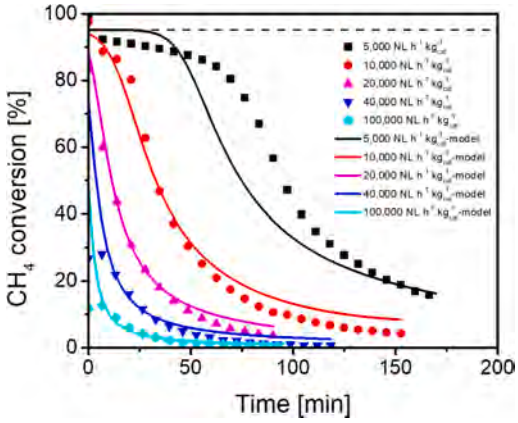

Fig. 6. Effect of GHSV on CH_4 conversion over time feeding CH_4 = 40% *v*/v, N_2 to balance at atmospheric pressure, T = 800 °C, GHSV = 5000; 10,000; 20,000; 40,000; 100,000 L(NTP) h^{-1} kg_{cat}^{-1}. Experimental data (symbols) and calculated results (solid lines). Thermodynamic equilibrium CH_4 conversion (dashed line) is also reported.

from the experimentally measured $C_{reactor}$, which accounts instead for the global carbon accumulation across the entire reactor. The relationship between C_{local} and $C_{reactor}$ is shown in **Eq. (6)**. Therefore, the formulation of activity function is inherently intrinsic and expectedly predictive, being a local function the solid properties and thus varying along the reactor axis.

$$C_{reactor}(t) = \int_{w1,reactor\ inlet}^{w2,reactor\ outlet} C_{local}(t)dw \text{ with } w1 = 0; w2 = W_{tot} \quad (6)$$

Eq. (5) represents a modification of the simple exponential model $a = \exp(-k_d C_{local})$ [54,55] in order to account for a residual non null catalyst activity a_∞. From **Eq. (5)**, the deactivation rate expression reported in Table 2 is easily obtained (detailed mathematical steps are reported in the Supplementary Information, **Section SI.2.6**).

Concerning the effect of temperature, activation energies were estimated by data fitting for the intrinsic parameters kp and kd; the activation energy of methane pyrolysis was found to be 160 kJ mol^{-1}, in agreement with previous studies reported in the literature [48], while the activation energy for the deactivation was estimated at 77 kJ mol^{-1}.

Once estimated the kinetic parameters, the assumptions underlying the one-dimensional description of the system were verified a posteriori. In particular, the absence of significant interphase temperature and concentration gradients, of intraparticle mass-transfer limitations, and of axial dispersion effects was verified. Details are reported in the Supplementary Information, **Sections SI.1.1 – SI.1.5.**

Results of the model regression are compared with the experimental data in Figs. 3–6, revealing a very satisfactory description of the effect of operating conditions on methane conversion, hydrogen productivity, and overall $C_{reactor}$ in the reactor. In particular, the model well reproduces the effect of methane concentration and the complex influence of temperature, with both the highest initial conversion and fastest catalyst deactivation observed at the maximum temperature of 800 °C, while lower temperatures result in lower initial conversion but slower deactivation. The model can reproduce such a trend (that brings to a negative temperature dependence at sufficiently long time on stream, or sufficiently high C_{local}) through the temperature dependence of both pyrolysis and deactivation activity constants.

In particular, the temperature dependence of the k_d is such that the activity declines with C_{local} with increasing sensitivity at increasing temperature, as more clearly highlighted in Fig. 8a that maps the functional dependences of the particle activity. Slices of the surface map at four different temperatures are instead shown in Fig. 8b**.**

Preliminary characterization results from an on-going study in fluidized bed reactor and reports from the literature bring to believe that this temperature-dependent deactivation behavior is intrinsically related to the temperature dependence of the modes of carbon structuring during the reaction. Indeed, in our previous study on the characterization and screening of Fe/Al_2O_3 catalysts, we have documented the wide variety of C-structures that characterize the process (micrographs form spent catalyst samples collected at low C-load are reported in **Fig. SI.10**); these include bamboo-like C-structures and multiwall nanotubes stemming from Fe_3C particles as well as onion-like C-layers covering the catalyst particles [40]. In particular, at lower temperatures the deposition of filamentous carbon and carbon nanotubes would predominate. These structures would allow a more continuous process of methane activation and carbon growth with limited loss of active sites and prolonged catalyst lifetime. At higher temperatures, the formation of encapsulating carbon would lead instead to a rapid loss of catalytic activity by blocking iron active sites [42,56].

The developed kinetic model has been validated by simulating in a predictive way the experiments at varying GHSV at two different operating temperatures (750 °C and 800 °C), shown in Fig. 6a and **Fig. SI.9** of the Supplementary Information. At both temperatures, reactor and kinetic models well reproduce the increased resistance to deactivation at decreasing space velocity. In addition, the temperature-dependence is well described, with more rapid decline of conversion at 800 °C, and a more gradual decline at 750 °C.

Table 2
Kinetic expressions and parameters.

	Rate equation	$k_j(1073\ K)$	$E_{act,j}$	a_∞
Initial pyrolysis rate	$r_p^0 = k_p P_{CH4}$	1.3 [mol kg_{catR}^{-1} s^{-1} atm^{-1}]	160 [kJ mol^{-1}]	
Deactivation rate	$r_d = k_d\, r_p (a - a_\infty) MM_c$	2.7 [g_C g_{catR}^{-1}]	77 [kJ mol^{-1}]	0.001

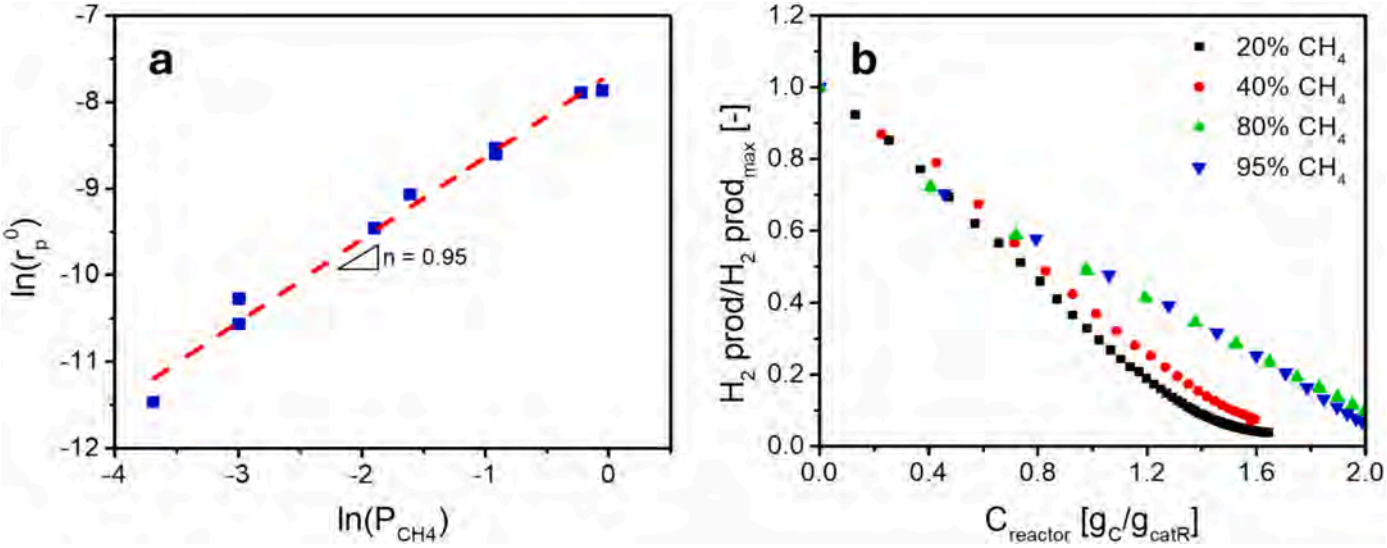

Fig. 7. (a) Linear fitting of experimental tests carried out at 800 °C, GHSV = 20,000 L(NTP) h^{-1} kg_{cat}^{-1} and inlet CH_4 concentration ranging from 2.5% to 95% *v*/v. (b) Normalized H_2 productivity with respect to the maximum H_2 productivity as a function of solid carbon accumulation. Operating conditions: T = 800 °C, GHSV = 20,000 L(NTP) h^{-1} kg_{cat}^{-1}. CH_4 = 20, 40, 80, 95% v/v, N_2 to balance, atmospheric pressure.

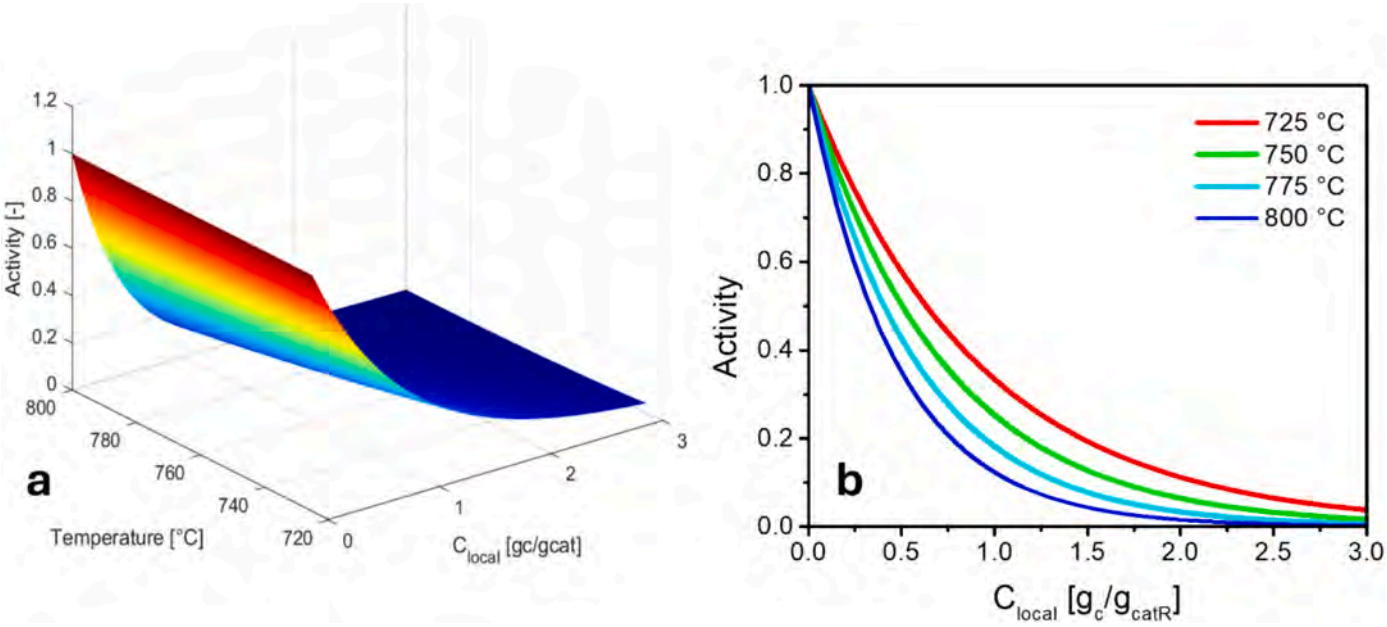

Fig. 8. (a) Surface map representing the evolution of catalyst activity (z axis) with temperature (y axis) and carbon build-up (x axis). (b) Section of the surface map at temperatures of 725 °C, 750 °C, 775 °C and 800 °C, where the y axis represents the catalyst activity and the x axis represents carbon build-up.

The model also reproduces the experimental trends observed at high space velocities (40,000 and 100,000 L(NTP) h^{-1} kg_{cat}^{-1}), except for the initial few minutes of reaction. As discussed in **Section 4.1.3**, a dwell in methane conversion is experimentally observed during this initial period, which is attributed to the formation of iron carbide (Fe_3C), a metastable intermediate that acts as the active phase in methane pyrolysis. These phenomena are not captured by the current reactor model, where the formation and transient impact of Fe_3C are not explicitly modelled. A detailed kinetic scheme, including the stepwise formation of iron carbide and its role in catalytic activity, would be required to resolve this deviation and provide an accurate description of the early-stage reactivity under differential conditions.

Less accurate is instead the prediction of the data collected at the lowest space velocity; as better shown in the following, this condition is expected to result in strongly non-homogenous carbon accumulation profile across the catalytic bed, generating a complex experimental and modelling case. Still, the general good prediction of the effect of GHSV on the reactor response is highly satisfactory.

4.3. PBR reactor analysis: spatio-temporal evolution of carbon deposition

By coupling the reactor model with the derived kinetic model, an insight of the fixed bed reactor behavior can be performed with focus on process variables that are not directly measurable. For instance, the model provides the distribution of carbon deposition along the reactor axis and the spatial variation of catalyst activity, which cannot be obtained experimentally. Surface maps were reconstructed to show the temporal evolution of the local carbon build-up across the catalyst bed for different operating conditions.

For example, Fig. 9a resents a three-dimensional map of the spatial

and temporal evolution of carbon when the reactor is fed with 95% CH_4 and operated at 800 °C, atmospheric pressure, GHSV of 20,000 L(NTP) h^{-1} kg_{cat}^{-1}. Axial profiles can be extracted by intersecting the surface at given times; an extensive analysis of characteristic C-distributions is proposed in **Section SI.2.8** of the Supplementary Information (**Figs. SI.11–15**) at varying operating conditions. Fig. 9b highlights in particular the important effect of space velocity on the C-distribution, by comparing the calculated C_{local} at 10 min from the start of the process.

It is observed that at decreasing GHSV from 20,000 to 5000 L(NTP) h^{-1} kg_{cat}^{-1} the predicted C-distribution profile is steeper thus less uniform, with pronounced accumulation near the reactor inlet. This effect is attributed to the lower methane flow rate, which results in higher local conversion in the upstream section and accelerates catalyst deactivation in that region.

Instead, by running the experiments of methane pyrolysis at high GHSV, more homogeneous C-profiles are expected across the bed in line with the approach to a differential reactor regime.

These results have interesting implications about the operation of the reactor and the accessibility of the kinetic information from the reactor response. High space velocities can put the operation of the reactor at a higher risk of rapid pressure build-up; however, they provide the more convenient access to kinetically relevant information. Low space velocities are safe from the point of view of the reactor operation, but the tendency to produce a large gradient of C-deposit can introduce the risk of case-specific C-growth phenomena in the bed and thus less rigorous kinetic content of the data. Not surprisingly, thus, the lowest space velocities are the experimental conditions where some lack of accuracy of the model prediction have been observed.

4.4. Model-guided experiments with pre-coking

In order to verify the model ability to describe the effect of space velocity under more uniform C-distributions across the bed new experiments were carried out on purpose by applying an initial "pre-coking" step to the catalyst, i.e., a conditioning phase at a GHSV of 20,000 L (NTP) h^{-1} kg_{cat}^{-1} of variable duration, ranging from short treatments of 3–4 min up to over 90 min, before switching to lower GHSV values. This approach aimed to investigate the performance of the catalyst in methane pyrolysis starting from a partially deactivated state, where an initial homogeneous carbon accumulation had already established.

In this context, Fig. 10 presents the results of three experiments in which a gas mixture containing 40% CH_4 balanced with N_2 was fed into the reactor at 800 °C. In all cases, pre-coking was carried out at a GHSV of 20,000 L(NTP) h^{-1} kg_{cat}^{-1}, followed by a reduction to different values: 2000 L(NTP) h^{-1} kg_{cat}^{-1} after 12 min (**black trend in** Fig. 10) 5000 L (NTP) h^{-1} kg_{cat}^{-1} after 3.5 min (**black trend in** Fig. 10) 10,000 L(NTP) h^{-1} kg_{cat}^{-1} after 12 min (**blue trend in** Fig. 10). In each case, a sharp increase of methane conversion was observed immediately after the GHSV switch. The simulation of the lower space velocity phase of the run was accurate, even at space velocity as low as 2000 L(NTP) h^{-1} kg_{cat}^{-1}. The same pre-coking strategy was also tested at 750 °C, and the comparison with the corresponding experiment at 800 °C is reported in Supplementary Information, **Fig. SI.16**.

In all cases, the model successfully captures the behavior of the system, accurately predicting the three key performance indicators: methane conversion (Fig. 10a), hydrogen productivity (Fig. 10b) and calculated $C_{reactor}$ (see Supplementary Information, **Fig. SI.17**), thereby confirming the robustness of the previously estimated kinetic parameters.

Additional experiments involving an initial pre-coking step are reported in the Supplementary Information, **Figs. SI.18** and **SI.19**, where the GHSV switch has been done after 12 min passing from 20,000 L (NTP) h^{-1} kg_{cat}^{-1} to 5000 L(NTP) h^{-1} kg_{cat}^{-1} and 10,000 L(NTP) h^{-1} kg_{cat}^{-1}, respectively. As in the case described Figure, the model accurately reproduced the experimental data also for the experiments shown in **Figs. SI.18** and **SI.19**. Other validation experiments were also performed by varying both the space velocity and inlet methane concentration as reported in the Supplementary Information, **Figs. SI.20** and **SI.21**, showing similar agreement between model and experimental results.

Another example of GHSV staging strategy is then reported in Fig. 11 where the gas mixture was initially fed at a GHSV of 20,000 L(NTP) h^{-1} kg_{cat}^{-1}, then reduced to 2000 L(NTP) h^{-1} kg_{cat}^{-1} after 91 min. By this time, the catalyst was consistently deactivated. As a result, the increase of methane conversion is less pronounced than in the pre-coking series of Fig. 10 (**black trend**), where pre-coking only lasted 12 min.

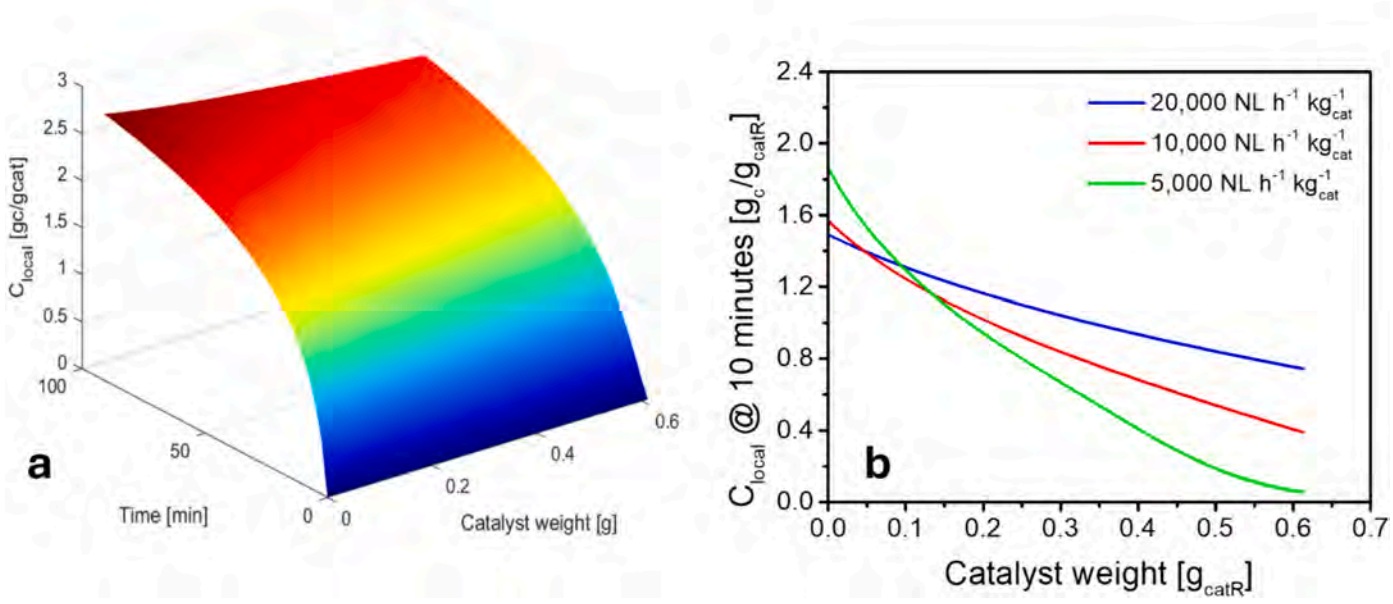

Fig. 9. (a) Surface map representing the evolution of carbon build-up (z axis) over time (y axis) along the reactor axis (x axis) for a test conducted under the following operating conditions: GHSV = 20,000 L(NTP) h^{-1} $kgcat^{-1}$, temperature = 800 °C, atmospheric pressure, and 95% CH_4 balanced with N_2. (b) Section of the surface map at 10 min, for the same experimental test performed at three different GHSV values: 5000, 10,000 and 20,000 L(NTP) h^{-1} $kgcat^{-1}$. The y axis reports the carbon build-up, while the x axis represents the amount of catalyst, equivalent to the reactor's axial coordinate.

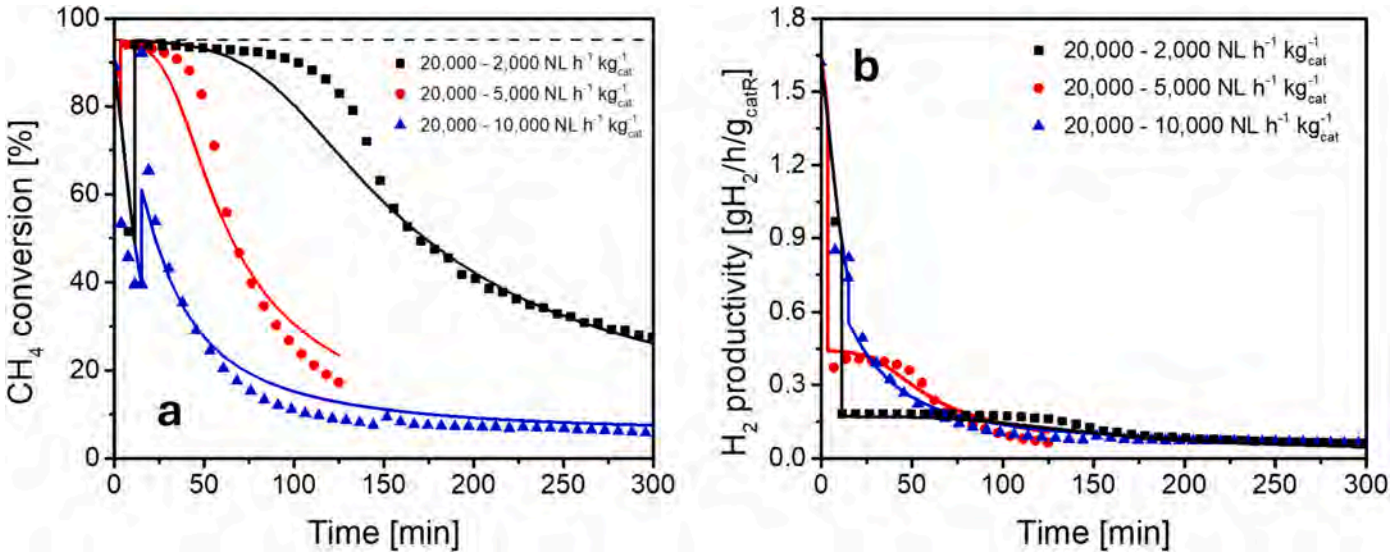

Fig. 10. Experimental data (symbols) and calculated results (solid lines) for CH_4 conversion and H_2 productivity are shown. Three cases are represented. (1) Operating conditions: GHSV = 20,000 (from 0 to 12 min), 10,000 (from 12 to 308 min) and 5000 (from 308 to 410 min) L(NTP) h^{-1} kg_{cat}^{-1}, CH_4 = 40% *v*/v, N_2 to balance, T = 800 °C, atmospheric pressure. (2) Operating conditions: GHSV = 20,000 (from 0 to 3.5 min) and 5000 (from 3.5 to 125 min) L(NTP) h^{-1} kg_{cat}^{-1}, CH_4 = 40% v/v, N_2 to balance, T = 800 °C, atmospheric pressure; (3) GHSV = 20,000 L(NTP) h^{-1} kg_{cat}^{-1} and CH_4 = 40% *v*/v (from 0 to 12 min), 2000 L(NTP) h^{-1} kg_{cat}^{-1} and CH_4 = 40% v/v (from 12 to 512 min) and 2000 L(NTP) h^{-1} kg_{cat}^{-1} and CH_4 = 80% v/v (from 512 to 570 min), N_2 to balance, T = 800 °C, atmospheric pressure.

Nonetheless, the model successfully captures the behavior of the system, accurately predicting the attenuated conversion response to the GHSV reduction, the lower carbon deposition rate and the flattened H_2 productivity trend. This confirms the model's ability to simulate dynamic operation starting from various initial catalyst states, a condition of great interest in relation to the possible realization of the pyrolysis process through a staging of reactors and thus of catalyst activity levels.

4.5. *Model-guided strategy for the maximization of C-load*

Still based on the results of the model analysis, experiments implementing a strategy of staged GHSV were then designed to experience the maximum carbon capacity of the catalyst, a key parameter for the economic sustainability of the methane pyrolysis process [41]. A gas mixture containing 80% CH_4 balanced with N_2 was fed at atmospheric pressure and fixed temperature of 780 °C, with progressively decreasing space velocity from the initial 5000 L(NTP) h^{-1} kg_{cat}^{-1} to 2000 L(NTP) h^{-1} kg_{cat}^{-1} and 1000 L(NTP) h^{-1} kg_{cat}^{-1}. Specifically, the GHSV was reduced by gradually decreasing the total flow rate at constant catalyst loading and inlet gas composition. Experimental results and model predictions, which satisfactorily reproduced the experimental behavior, are shown in Fig. 12. This strategy enhanced the CH_4 conversion (Fig. 12a), effectively limited the overpressure (see Supplementary Information, **Fig. SI.22**), and thus enabled prolonged operations, ultimately reaching the final $C_{reactor}$ of 5 g_C g_{cat}^{-1} after 1260 min of TOS (Fig. 12b).

This result is of particular relevance, since this very value of carbon

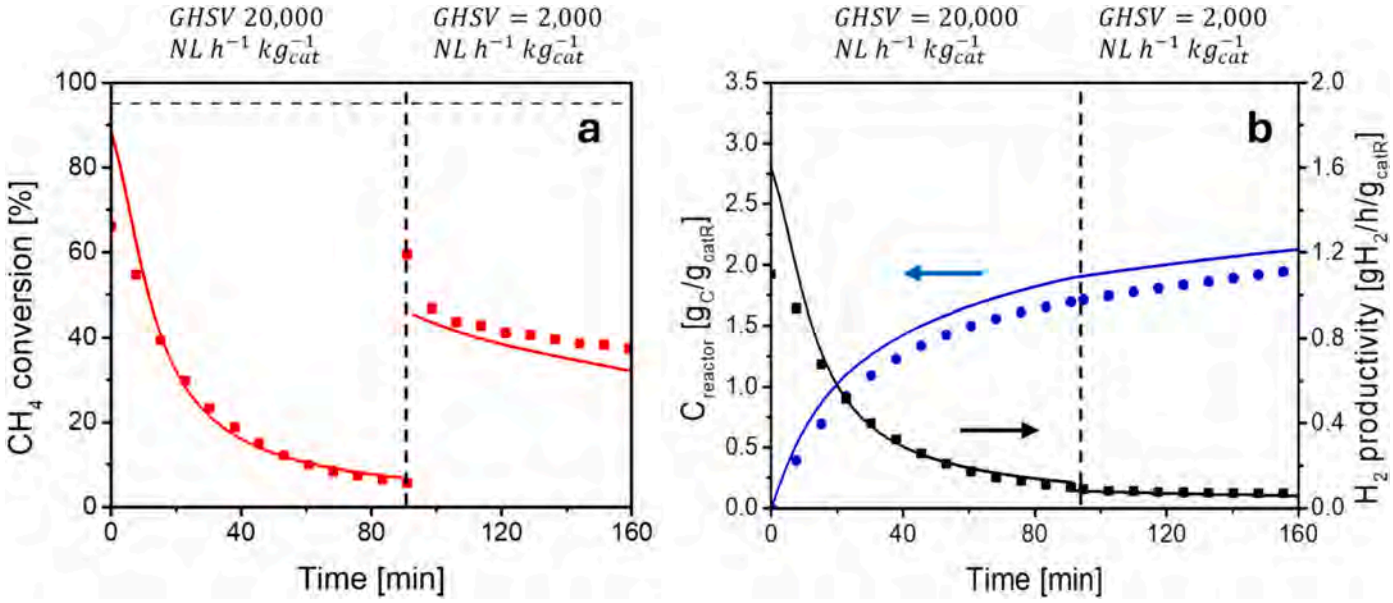

Fig. 11. Effect of GHSV on CH_4 conversion and solid carbon production. Experimental data (symbols) and calculated results (solid lines) for CH_4 conversion, carbon build-up and H_2 productivity are shown. Operating conditions: GHSV = 20,000 (from 0 to 92 min) and 2000 (from 92 to 160 min) L(NTP) h^{-1} kg_{cat}^{-1}, CH_4 = 40% v/v, N_2 to balance, temperature = 800 °C, atmospheric pressure.

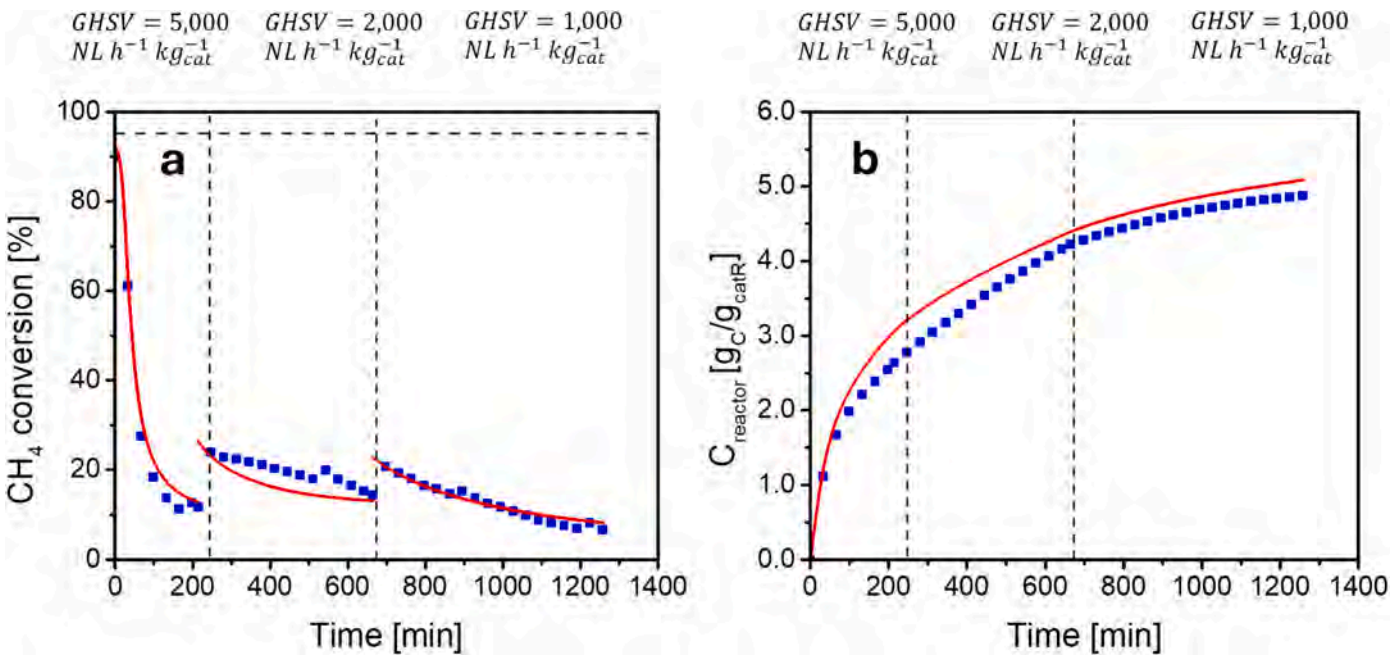

Fig. 12. Effect of GHSV on CH_4 conversion and solid carbon production. Experimental data (symbols) and calculated results (solid lines). Operating conditions: GHSV = 5000 L(NTP) h^{-1} kg_{cat}^{-1} (from 0 to 213 min), 2000 (from 213 to 665 min) and 1000 (from 665 to 1260 min) L(NTP) h^{-1} kg_{cat}^{-1}, CH_4 = 80% *v*/v, N_2 to balance, temperature = 780 °C, atmospheric pressure.

capacity has been identified by De Cataldo et al. [41] in their techno-economic analysis as one of the key factors (together with low natural gas prices, implementation in small- to medium-scale plants with relatively simple designs, and the use of low-cost catalysts) to make methane pyrolysis competitive with other blue-hydrogen technologies. Specifically, reported thresholds of $C_{reactor}$ of 5 g_C g_{cat}^{-1} for iron-based catalysts and 20 g_C g_{cat}^{-1} for nickel-based catalysts would be required to achieve viable operation. In this context, another crucial determinant is the valorization of the solid carbon co-product: the commercialization of high-value carbon materials (e.g., graphite, carbon nanotubes) can substantially improve process economics. Ultimately, the combination of robust catalyst performance, efficient carbon management, and favorable market or infrastructure conditions is essential to ensure the economic viability of methane pyrolysis.

5. Conclusive remarks

This work provides a comprehensive experimental and modelling study of methane pyrolysis over iron catalyst in a packed-bed reactor. Experimentally, the influence of key operating parameters such as temperature, methane concentration, and space velocity was systematically assessed in a wide range. Higher temperatures (800 °C) enhanced initial methane conversion but accelerated catalyst deactivation, while lower temperatures (725 °C) enabled higher $C_{reactor}$ to be achieved. Similarly, increasing methane concentration promoted carbon deposition but led to faster deactivation, whereas reducing the gas hourly space velocity favoured higher methane conversion and enabled up to 5 g_C g_{catR}^{-1}, consistent with thresholds reported for the economic viability of Fe-based systems. Finally, hydrogen co-feeding did not show any significant influence on methane conversion.

From a kinetic standpoint, the rate of methane decomposition was found to follow a first-order dependence on methane partial pressure, while catalyst deactivation was described by a carbon-dependent decay function that is emphasized by temperature. These findings explain the strong sensitivity of catalyst stability at elevated temperatures. The derived kinetic parameters were successfully implemented in a one-dimensional dynamic packed-bed reactor model, which accurately reproduced experimental results under a wide range of conditions and remained predictive when validated against independent datasets.

This work revealed that operating at high GHSV values the reactor operates close to a differential regime with uniform carbon growth, thus simplifying kinetic analysis and modelling. At large TOS, however, pressure drops may become an issue. Conversely, lower GHSV values allow for longer experimental runs without pressure build-ups, enabling the achievement of higher C-loads, but are more challenging to model analysis due to a highly non-uniform distribution of carbon load and activity along the reactor.

Overall, the combined experimental and modelling results provide a robust kinetic framework for methane pyrolysis, offering predictive capability for catalyst behavior and system performance. The proposed kinetic model can be integrated into reactor-scale models, such as those for fluidized-bed systems, thus supporting process optimization and scale-up toward industrial applications. We can here anticipate that the model is being successfully integrated in the dynamic Kunii-Levenspiel model of a lab-scale fluidized bed reactor, showing very good prediction of methane pyrolysis experiments over the same catalyst formulation; this serves as an important confirmation of the intrinsic nature of the proposed kinetic model. The results of this ongoing activity will be reported in future publications.

In summary, the kinetic model proposed this work pursues a practical balance between accuracy and simplicity, making it particularly suitable for engineering calculations on reactor and process schemes. Nonetheless, future research may benefit from integrating lumped and detailed kinetic approaches to enhance predictive capabilities while maintaining tractability in large-scale reactor modelling.

While the present work is mainly focused on process kinetics as a key requirement for reactor design, it is important to recall that carbon valorization is a crucial factor for the economic sustainability and thus the feasibility of the process. Since the selected Fe-Al_2O_3 catalyst gives rise to a variety of carbon structures without the selective formation of highly valuable carbon nanotubes, it is believed that the implementation of methane pyrolysis at large scale, hence large hydrogen and carbon, coupled with a non-specific carbon utilization strategy might be a successful route. For this purpose, the application of the C-Fe/Al_2O_3 spent catalysts for the preparation of carbon self-reducing agglomerates is being presently studied and will be reported in a forthcoming paper.

CRediT authorship contribution statement

Davide Cafaro: Writing – original draft, Validation, Methodology, Investigation, Formal analysis. **Marco Orsenigo:** Writing – original draft, Methodology, Investigation, Data curation. **Veronica Piazza:** Writing – review & editing, Methodology, Formal analysis, Data curation, Conceptualization. **Lidia Castoldi:** Writing – review & editing, Supervision, Methodology. **Flavio Lucini:** Supervision, Resources, Funding acquisition, Data curation. **Andrea Lainati:** Writing – review & editing, Supervision, Resources, Conceptualization. **Gianpiero Groppi:** Writing – review & editing, Supervision, Formal analysis, Conceptualization. **Matteo Maestri:** Writing – review & editing, Supervision, Methodology, Formal analysis, Conceptualization. **Alessandra Beretta:** Writing – review & editing, Validation, Supervision, Project administration, Methodology, Formal analysis, Data curation, Conceptualization.

Declaration of competing interest

The authors declare the following financial interests/personal relationships which may be considered as potential competing interests: Prof. Matteo Maestri, coauthor of the present manuscript, belongs to the Editorial Board of CEJ (Chemical Reaction Engineering) If there are other authors, they declare that they have no known competing financial interests or personal relationships that could have appeared to influence the work reported in this paper.

Appendix A. Supplementary data

Supplementary data to this article can be found online at https://doi.org/10.1016/j.cej.2026.178191.

Data availability

Data will be made available on request.

References

[1] F. Dawood, M. Anda, G.M. Shafiullah, Hydrogen production for energy: an overview, Int. J. Hydrog. Energy 45 (7) (2020) 3847–3869, https://doi.org/10.1016/j.ijhydene.2019.12.059.

[2] U.Y. Qazi, Future of hydrogen as an alternative fuel for next-generation industrial applications; challenges and expected opportunities, Energies (Basel) 15 (13) (2022), https://doi.org/10.3390/en15134741.

[3] A. Bakenne, W. Nuttall, N. Kazantzis, Sankey-Diagram-based insights into the hydrogen economy of today, Int. J. Hydrog. Energy 41 (19) (2016) 7744–7753, https://doi.org/10.1016/j.ijhydene.2015.12.216.

[4] D. Hart, et al., Scenarios for Deployment of Hydrogen in Contributing to Meeting Carbon Budgets and the 2050 Target, 2015.

[5] I. Energy Agency, Global Hydrogen Review 2024 [Online]. Available: www.iea.org, 2024.

[6] L. Weger, A. Abánades, T. Butler, Methane cracking as a bridge technology to the hydrogen economy, Int. J. Hydrog. Energy 42 (1) (2017) 720–731, https://doi.org/10.1016/j.ijhydene.2016.11.029.

[7] T.I. Korányi, M. Németh, A. Beck, A. Horváth, Recent advances in methane pyrolysis: turquoise hydrogen with solid carbon production, Energies (2022), https://doi.org/10.3390/en15176342.

[8] A.O. Oni, K. Anaya, T. Giwa, G. Di Lullo, A. Kumar, Comparative assessment of blue hydrogen from steam methane reforming, autothermal reforming, and natural gas decomposition technologies for natural gas-producing regions, Energy Convers. Manag. 254 (2022) 115245, https://doi.org/10.1016/j.enconman.2022.115245.

[9] B. Parkinson, P. Balcombe, J.F. Speirs, A.D. Hawkes, K. Hellgardt, Levelized cost of CO 2 mitigation from hydrogen production routes, Energy Environ. Sci. 12 (1) (2019) 19–40.

[10] S. Patel, How much will hydrogen-based power cost, *Publicado online en Powermag. com. Recuperado de:*, *https://www.powermag.com/how-much-will-hydrogen-based-power-cost/*, 2020. *Recurso Online*.

[11] U. Department of Energy Hydrogen and F. Cells Program, 2019 Annual Progress Report: DOE Hydrogen and Fuel Cells Program [Online]. Available: www.nrel.gov/publications, 2019.

[12] S.B. Harrison, Turquoise hydrogen production by methane pyrolysis, Digital Refining PTQ 4 (2021).

[13] O. Machhammer, A. Bode, W. Hormuth, Financial and ecological evaluation of hydrogen production processes on large scale, Chem. Eng. Technol. 39 (6) (2016) 1185–1193.

[14] N. Sánchez-Bastardo, R. Schlögl, H. Ruland, Methane pyrolysis for zero-emission hydrogen production: a potential bridge technology from fossil fuels to a renewable and sustainable hydrogen economy, Ind. Eng. Chem. Res. 60 (32) (2021) 11855–11881, https://doi.org/10.1021/acs.iecr.1c01679.

[15] R. Paul, et al., 3D heteroatom-doped carbon nanomaterials as multifunctional metal-free catalysts for integrated energy devices, Adv. Mater. 31 (13) (2019) 1805598.

[16] R. Utrilla, J.L. Pinilla, I. Suelves, M.J. Lázaro, R. Moliner, Catalytic decomposition of methane for the simultaneous co-production of CO2-free hydrogen and carbon nanofibre based polymers, Fuel 90 (1) (2011) 430–432.

[17] V. Selamneni, N. Bokka, V. Adepu, P. Sahatiya, Carbon nanomaterials for emerging electronic devices and sensors, in: Carbon Nanomaterial Electronics: Devices and Applications, Springer, 2021, pp. 215–258.

[18] R. Rao, et al., Carbon nanotubes and related nanomaterials: critical advances and challenges for synthesis toward mainstream commercial applications, ACS Nano 12 (12) (2018) 11756–11784.

[19] M. Pasquali, C. Mesters, We can use carbon to decarbonize—and get hydrogen for free, Proc. Natl. Acad. Sci. 118 (31) (2021) e2112089118.

[20] M. Orsenigo *et al.*, n.d. "Methane Pyrolysis in Fluidized Bed Reactor for the Simultaneous Production of Low-C Hydrogen and Carbon Materials for the Steel Industry", in preparation.

[21] N. Muradov, F. Smith, C. Huang, A. T-Raissi, Autothermal catalytic pyrolysis of methane as a new route to hydrogen production with reduced CO2 emissions, Catal. Today 116 (3) (2006) 281–288.

[22] N.Z. Muradov, T.N. Veziroğlu, From hydrocarbon to hydrogen–carbon to hydrogen economy, Int. J. Hydrog. Energy 30 (3) (2005) 225–237.

[23] H.F. Abbas, W.M.A.W. Daud, Hydrogen production by methane decomposition: a review, Int. J. Hydrog. Energy 35 (3) (2010) 1160–1190.

[24] A.E. Awadallah, A.A. Aboul-Enein, A.K. Aboul-Gheit, Effect of progressive Co loading on commercial Co–Mo/Al2O3 catalyst for natural gas decomposition to COx-free hydrogen production and carbon nanotubes, Energy Convers. Manag. 77 (2014) 143–151.

[25] Y. Li, J. Chen, Y. Qin, L. Chang, Simultaneous production of hydrogen and nanocarbon from decomposition of methane on a nickel-based catalyst, Energy Fuel 14 (6) (2000) 1188–1194.

[26] M. Pudukudy, Z. Yaakob, Z.S. Akmal, Direct decomposition of methane over SBA-15 supported Ni, Co and Fe based bimetallic catalysts, Appl. Surf. Sci. 330 (2015) 418–430.

[27] N. Sánchez-Bastardo, R. Schlögl, H. Ruland, Methane pyrolysis for co2-free h2 production: a green process to overcome renewable energies unsteadiness, Chem. Ing. Tech. 92 (10) (2020) 1596–1609.

[28] R.R.C.M. Silva, et al., Effect of support on methane decomposition for hydrogen production over cobalt catalysts, Int. J. Hydrog. Energy 41 (16) (2016) 6763–6772.

[29] S.R. Patlolla, K. Katsu, A. Sharafian, K. Wei, O.E. Herrera, W. Mérida, A review of methane pyrolysis technologies for hydrogen production, Renew. Sust. Energ. Rev. 181 (2023) 113323.

[30] U.P.M. Ashik, W.M.A.W. Daud, H.F. Abbas, Production of greenhouse gas free hydrogen by thermocatalytic decomposition of methane–a review, Renew. Sust. Energ. Rev. 44 (2015) 221–256.

[31] G. Wang, Y. Jin, G. Liu, Y. Li, Production of hydrogen and nanocarbon from catalytic decomposition of methane over a Ni–Fe/Al2O3 catalyst, Energy Fuel 27 (8) (2013) 4448–4456.

[32] S. Takenaka, M. Serizawa, K. Otsuka, Formation of filamentous carbons over supported Fe catalysts through methane decomposition, J. Catal. 222 (2) (2004) 520–531.

[33] M.A. Ermakova, D.Y. Ermakov, A.L. Chuvilin, G.G. Kuvshinov, Decomposition of methane over iron catalysts at the range of moderate temperatures: the influence of structure of the catalytic systems and the reaction conditions on the yield of carbon and morphology of carbon filaments, J. Catal. 201 (2) (2001) 183–197.

[34] H.J. Grabke, Evidence on the surface concentration of carbon on gamma iron from the kinetics of the carburization in CH4− H2, Metall. Trans. A. 1 (10) (1970) 2972–2975.

[35] I. Suelves, M.J. Lázaro, R. Moliner, B.M. Corbella, J.M. Palacios, Hydrogen production by thermo catalytic decomposition of methane on Ni-based catalysts: influence of operating conditions on catalyst deactivation and carbon characteristics, Int. J. Hydrog. Energy 30 (15) (2005) 1555–1567.

[36] S. Geng, et al., Methane decomposition kinetics over Fe2O3 catalyst in micro fluidized bed reaction analyzer, Ind. Eng. Chem. Res. 57 (25) (2018) 8413–8423.

[37] M. Keller, A. Matsumura, A. Sharma, Spray-dried Fe/Al2O3 as a carbon carrier for COx-free hydrogen production via methane cracking in a fluidized bed process, Chem. Eng. J. 398 (2020) 125612.

[38] R. Siriwardane, J. Riley, C. Atallah, M. Bobek, Investigation of methane and ethane pyrolysis with highly active and durable iron-alumina catalyst to produce hydrogen and valuable nano carbons: Continuous fluidized bed tests and reaction rate analysis, Int. J. Hydrog. Energy 48 (38) (2023) 14210–14225.

[39] P. Vedele, et al., Thermocatalytic methane pyrolysis over iron-based catalysts for turquoise hydrogen production: activity and kinetic studies, Chem. Eng. J. 514 (2025) 163392.

[40] C. Negri, V. Piazza, M. Orsenigo, M. Maestri, G. Groppi, L. Castoldi, A. Beretta, Methane pyrolysis on fused Fe-Al2O3 catalysts: Characterization of catalyst structure, performance and carbon formation, Appl. Catal. A, Gen. 711 (2026) 120719.

[41] A. De Cataldo, et al., Blueish hydrogen production via methane pyrolysis and remote CO2 capture and storage, Int. J. Hydrog. Energy 146 (2025) 149723.
[42] J.L. Pinilla, et al., High temperature iron-based catalysts for hydrogen and nanostructured carbon production by methane decomposition, Int. J. Hydrog. Energy 36 (13) (2011) 7832–7843.
[43] P. Forzatti, L. Lietti, Catalyst deactivation, Catal. Today 52 (2–3) (1999) 165–181.
[44] J.H. Perry, Chemical engineers' handbook, J. Chem. Educ. 27 (1950). ACS Publications.
[45] MathWorks, fsolve — Solve system of nonlinear equations, in: Optimization Toolbox, 2025 [Online]. Available: https://www.mathworks.com/help/optim/ug/fsolve.html.
[46] D. Torres Gamarra, S. de Llobet, J.L. Pinilla Ibarz, M.J. Lázaro Elorri, I. Suelves Laiglesia, R. Moliner Álvarez, Hydrogen Production by Catalytic Decomposition of Methane Using a Fe-based Catalyst in a Fluidized Bed Reactor, 2012.
[47] J.X. Qian, et al., Optimization of a fluidized bed reactor for methane decomposition over Fe/Al2O3 catalysts: Activity and regeneration studies, Int. J. Hydrog. Energy 44 (60) (2019) 31700–31711, https://doi.org/10.1016/j.ijhydene.2019.10.058.
[48] W. Arabczyk, et al., Kinetics of the iron carbide formation in the reaction of methane with nanocrystalline iron catalyst, Appl. Catal. A Gen. 266 (2004) 135–145.
[49] L. Zhou, et al., Fe catalysts for methane decomposition to produce hydrogen and carbon nano materials, Appl. Catal. B 208 (2017) 44–59.
[50] T. Keipi, Technology development and techno-economic analysis of hydrogen production by thermal decomposition of methane, 2017.
[51] D.-C. Toncu, G. Toncu, S. Soleimani, On methane pyrolysis special applications, IOP. Conf. Ser. Mater. Sci. Eng. (2015) 012026. IOP Publishing.
[52] S. Rodat, S. Abanades, J. Coulié, G. Flamant, Kinetic modelling of methane decomposition in a tubular solar reactor, Chem. Eng. J. 146 (1) (2009) 120–127.
[53] S.H. Sharif Zein, A.R. Mohamed, P.S. Talpa Sai, Kinetic studies on catalytic decomposition of methane to hydrogen and carbon over Ni/TiO2 catalyst, Ind. Eng. Chem. Res. 43 (16) (2004) 4864–4870.
[54] Z.M. Shakor, E.N. Al-Shafei, The mathematical catalyst deactivation models: a mini review, Royal Society of Chemistry (Jul. 26, 2023), https://doi.org/10.1039/d3ra02912c.
[55] F.J. Dumez, G.F. Froment, Dehydrogenation of 1-Butene into Butadiene. Kinetics, Catalyst Coking, and Reactor Design, Ind. Eng. Chem., Process Des. Dev. 15 (2) (1976) 291–301.
[56] I. Suelves, J.L. Pinilla, M.J. Lázaro, R. Moliner, J.M. Palacios, Effects of reaction conditions on hydrogen production and carbon nanofiber properties generated by methane decomposition in a fixed bed reactor using a NiCuAl catalyst, J. Power Sources 192 (1) (2009) 35–42.